Matter

CellPress

Article

All-protein-based rewritable and reprogrammable multifunctional optical imaging platforms via multi-strategy imprinting and multimode 3D morphing

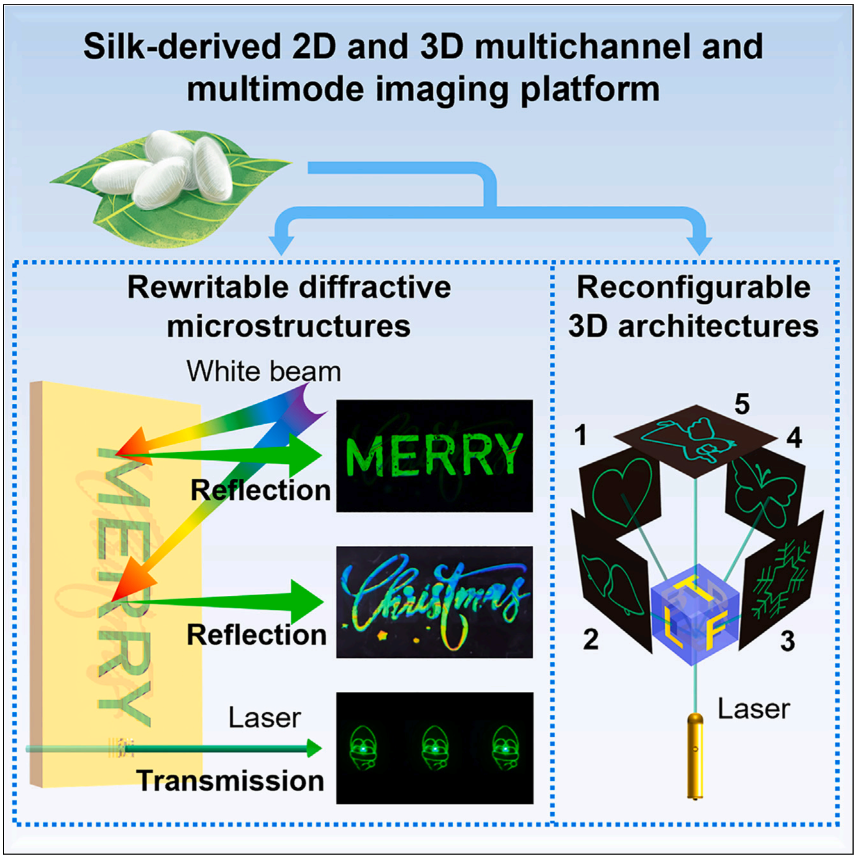

Jiang et al. developed a multifunctional optical imaging platform by endowing a silk-protein-based film with diverse micro-/nanostructures using a multi-strategy imprinting technique and morphing it into a 3D shape assisted by origami/kirigami. It achieves the integration of several imaging channels within a single biocompatible matrix in both 2D and 3D geometries and features unique advantages by being optically rewritable and structurally reprogrammable. Applications of the platform as high-security anti-counterfeiting labels, 3D multidirectional display devices, and advanced 3D encryption devices are demonstrated.

4

Demonstrate

Proof-of-concept of performance with intended application/response

Chang Jiang, Tao Wang, Yinghao Fu, Peng Chen, Guangming Tao, Yu Wang, Yanqing Lu

yuwang87@nju.edu.cn (Y.W.)
yqlu@nju.edu.cn (Y.L.)

Highlights

Construct multifunctional optical imaging platforms using versatile silk proteins

The micro-/nanostructures can be rewritten and the 3D shape can be reprogrammed

Create anti-counterfeiting labels with enhanced security levels

Integrate multidirectional color display and holography in a single device

Jiang et al., Matter 7, 1591–1611
April 3, 2024 © 2024 Elsevier Inc.
https://doi.org/10.1016/j.matt.2024.01.030

Matter

CellPress

Article

All-protein-based rewritable and reprogrammable multifunctional optical imaging platforms via multi-strategy imprinting and multimode 3D morphing

Chang Jiang,[1] Tao Wang,[1] Yinghao Fu,[1] Peng Chen,[1] Guangming Tao,[2] Yu Wang,[1,3,*] and Yanqing Lu[1,*]

SUMMARY

Optical imaging devices with multiple distinct functionalities are becoming increasingly important for smart displays, high-security encryption, and multilevel anti-counterfeiting applications. However, existing systems are often challenging to reconfigure once formed and lack 3D encoding capacity. Here, we present a protein-based approach to construct rewritable and reprogrammable multifunctional optical platforms that allow 2D/3D encoding, multichannel imaging, and multimode information multiplexing by combining protein self-assembly, micro-/nanoimprinting, and 3D morphing techniques. The use of multi-strategy imprinting enables the encoding of multiple independent optical responses in one material, while the incorporation of 3D architecture offers additional spatial freedom for information integration. The protein's ability for reversible molecular rearrangement allows the rewriting of imprinted optical structures and the reconfiguration of 3D geometries, providing access to reusable adaptive optical imaging platforms. We present various demonstrator devices, including multistage encryption, multilayer anti-counterfeiting, 3D multidirectional display, and high-level 3D encryption, to illustrate the platform's versatile utility.

INTRODUCTION

Traditional optical devices designed for optical imaging have been successful in achieving well-tailored and high-quality single functions through careful engineering of the constituent materials. However, the ever-increasing demands for optical imaging systems in areas such as smart displays, high-capacity information storage, high-security encryption, and multilevel anti-counterfeiting have promoted the need for optical materials and devices that can provide multiple functionalities to transmit distinct optical signals and handle concurrent tasks. Researchers are exploring new technologies for the integrated design of optical devices to address this need.[1–6] Optical multiplexing technology is a concept of integrating multiple information channels into one platform and displaying each piece of information individually under the corresponding external stimuli,[1,2,7–9] providing new opportunities to replace single-function imaging devices with multifunctional integrated systems that match the high quality of traditional devices while improving intelligence, storage capacity, and decryption difficulty.

Significant efforts have been devoted to developing advanced optical multiplexing technologies for multifunctional designs in recent years. The most prevalent technology involves metasurfaces, which can precisely manipulate light flow from multiple dimensions (such as amplitude, phase, and polarization). By encoding different

PROGRESS AND POTENTIAL

Multifunctional optical imaging devices serving diverse purposes in displays, information encryption, and anti-counterfeiting are in high demand. However, creating systems with the ability to reconfigure and encode information in 3D space is still challenging. In this work, silk-protein-based multifunctional optical platforms capable of generating reprogrammable optical images in 2D/3D are developed. The exploitation of multi-strategy imprinting enables the integration of multiple independent optical responses in a 2D plane, and the introduction of the morphing technique allows information encoding in 3D space. The resulting platform combines a multitude of advantageous features, including sustainability, biocompatibility, biodegradability, excellent adhesion property, rewritability, and reprogrammability, in a versatile protein format. These convergent functions offer potential applications in smart displays, high-security encryption, and multilevel anti-counterfeiting.

information into different dimensions, a wide variety of multiplexing and multifunctional metasurfaces have been designed.[5,10–18] Another effective technology to enrich optical information relies on color- and lifetime-tunable luminescent materials, which are capable of creating spatial and temporal coding dimensions by manipulating luminescence wavelengths and decay lifetimes.[19–25] Photonic crystals can also provide a strategy for information multiplexing through hierarchical design[26,27] or the introduction of multiple responsive components.[23,28–31] Recently, liquid-crystal-based multifunctional devices that simultaneously display surface grayscale patterns and wavelength-multiplexed holographic images by separately manipulating the amplitude and phase of incident light have also been demonstrated.[32,33] Despite these remarkable advances toward multifunctionality, these multiplexing technologies often rely on complex and energy-intensive fabrication and encoding procedures. The resulting platforms, once encoded, are usually non-reconfigurable and unable to form new multiplexed functions, which can be disadvantageous in terms of material reusability, sustainability, and information renewal and substitution. Additionally, existing optical multiplexing technologies primarily encode information onto single two-dimensional (2D) planar platforms and are incapable of manipulating light in three-dimensional (3D) space, limiting the encoding of information in the third dimension. The introduction of a spatial degree of freedom by constructing 3D optical platforms is beneficial for increasing storage density, imaging dimension, and encryption level.[34,35] Therefore, there is a need to develop new multiplexing technology that can create rewritable and reprogrammable multifunctional optical platforms with imaging capacities in both two and three dimensions through straightforward, green, and scalable fabrication and encoding methodologies.

We describe here the use of naturally derived silk protein as the building blocks to fabricate multifunctional optical platforms that are capable of multichannel and multimode imaging in 2D/3D space based on rewritable 2D optical structures and reconfigurable 3D geometries. The selection of silk protein as the construction material for optical imaging is driven by its remarkable convergence of diverse material characteristics, including sustainable sourcing, hierarchical and tailorable structures, stimuli responsiveness, multilevel processability, favorable optical properties, mechanical robustness, and ease of functionalization. It is presented that a variety of composite optical structures can be written onto a 2D platform by leveraging scalable, spatial-controllable, and multi-strategy micro-/nanoimprinting techniques. This 2D plane can be further shaped into multimodal and complex 3D architectures that provide additional channels for information multiplexing using morphing techniques assisted by origami designs. We demonstrate that both the printed optical structures and 3D configuration can be redefined as a result of the reversible molecular rearrangement of silk protein induced by water vapor. Finally, we demonstrate that this highly integrated platform can be utilized as security labels that encrypt information in a multistage or multilayer manner and as 3D devices for multidirectional information display and high-level encryption. We believe that the investigated optical platforms exhibit notable advantages over conventional optical systems, in terms of not only environmental friendliness, biocompatibility, and biodegradability but also efficient manufacturing processes, flexible integration of micro-/nanostructures, rewritability, and reprogrammable 3D multiplexing capabilities (as summarized in Table S1).

RESULTS

Multifunctional optical platform with multichannel design

The concept of the silk-protein-based multifunctional optical platform is depicted in Figures 1A and 1B. This platform offers the integration of multiple imaging channels

[1]National Laboratory of Solid State Microstructures, Key Laboratory of Intelligent Optical Sensing and Manipulation, College of Engineering and Applied Sciences, Collaborative Innovation Center of Advanced Microstructures, Nanjing University, Nanjing 210023, China

[2]Wuhan National Laboratory for Optoelectronics, State Key Laboratory of Material Processing and Die & Mould Technology, School of Materials Science and Engineering, Huazhong University of Science and Technology, Wuhan 430074, China

[3]Lead contact

*Correspondence: yuwang87@nju.edu.cn (Y.W.), yqlu@nju.edu.cn (Y.L.)

https://doi.org/10.1016/j.matt.2024.01.030

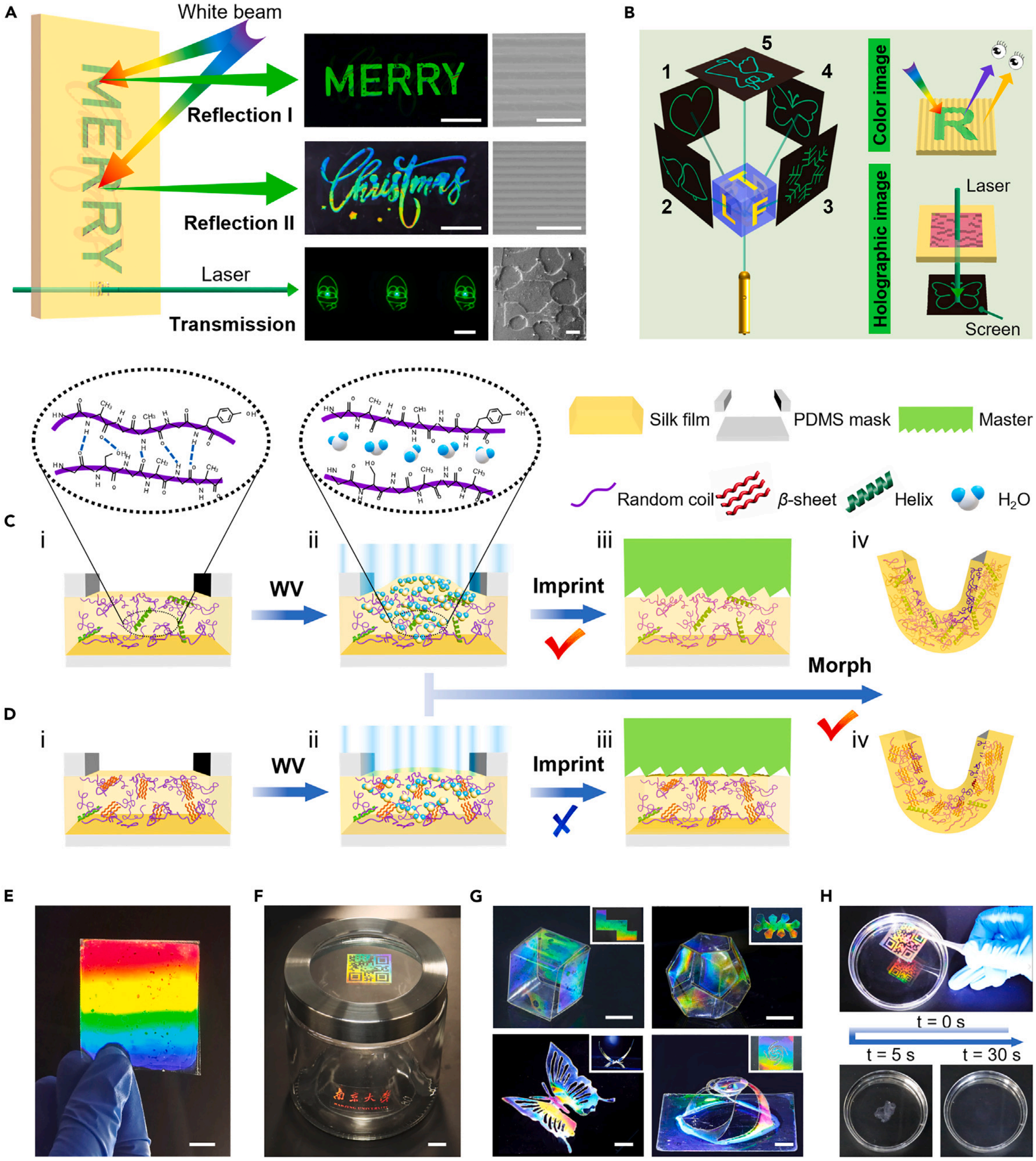

Figure 1. Concept, mechanism, and properties of silk-based multifunctional optical imaging platform

(A) Schematic and photographs of a silk-film-based 2D multifunctional platform that simultaneously stores independent images in different channels (RC, reflection channel; TC, transmission channel). Scale bars, 1 cm (left) and 5 µm (right).

(B) Schematic illustration of a spatial multidirectional imaging device that integrates color display and holography by modulating reflection and transmission responses simultaneously.

(C and D) Schematics showing the mechanism of water-vapor-enabled micro-/nanoimprinting (i, ii, iii) and shape morphing (i, ii, iv) of amorphous (C) and crystalline (D) silk films. The enlarged insets show the breakage of hydrogen bonding between silk fibroin molecular chains after water-molecule infiltration.

(E) Photograph of a cm-scale (5 × 5 cm) free-standing silk film with nanoimprinted grating structure displaying bright iridescence. Scale bar, 1 cm.

(F) Photograph of two patterned films attached to the flat lid and curved body of a glass container. Scale bar, 1 cm.

(G) Photographs of colored silk films with complex 3D configurations. Insets: corresponding 2D precursors or side view. Scale bars, 5 mm.

(H) Photographs showing the rapid solubility (within 30 s) of an amorphous silk film encoded with a QR code in water.

within a single biocompatible matrix in both 2D and 3D geometries. In the 2D geometry, diverse images can be encoded in different illumination-viewing angles and modes. For example, in reflection mode, two color images, namely the "MERRY" pattern and the "Christmas" pattern, can be observed under different illumination/viewing angles. Meanwhile, in transmission mode, a holographic image displaying a series of Santa Claus patterns under laser irradiation can be seen (Figure 1A). In the 3D geometry, the additional spatial dimension allows further integration of the 2D encoded information. For instance, by shaping a dual-channel encoded silk matrix into a cube-shaped 3D structure, a multifaceted color image display and a multidirectional holographic display can be simultaneously achieved (Figure 1B).

The production of 2D multifunctional platforms is achieved through the utilization of micro-/nanoimprinting techniques. Imprinting methods have been shown to be effective for the rapid, scalable, and high-throughput generation of optical micro-/nanostructures on silk matrices, as reported in previous literature.[36,37] In this study, we improve the previously reported water-aided room-temperature embossing technique by developing a water-vapor-enabled imprinting method. This new technique provides improved capabilities for spatially controllable and multi-strategy imprinting. During the process, a silk film was fumigated with water vapor generated by heated water before positioning a master on its surface. Immediately thereafter, a constant pressure was applied on the master above the silk film to induce the reflow of "activated" protein chains into the grooves of the master, thereby replicating its topological micro-/nanostructure (Figure 1Ci–iii). The imprinted film was obtained after drying and removing the master. These 2D optically encoded substrates can be further transformed into various complex 3D architectures by adopting a water-vapor-triggered, origami-guided morphing technique. In this process, a polydimethylsiloxane (PDMS) mask was applied to the surface of a prefabricated 2D precursor, allowing for local infiltration of water vapor. Upon ceasing the fumigation and removing the binding, the free-standing precursor can undergo spontaneous bending at specifically exposed regions to adopt the intended 3D configuration (Figure S1 and Video S1). Different bending angles of 3D geometries could be achieved easily by controlling the duration of water-vapor fumigation (Figure S2).

The mechanism underlying the formation of micro-/nanoimprints and 3D architectures using water vapor can be understood by molecular chain softening and rearrangement induced by the interaction between water molecules and the polar groups of silk protein chains (Figures 1C and 1D).[38,39] During exposure, water molecules can penetrate the silk matrix and soften the silk protein chains by disrupting the hydrogen bonds between them (Figures 1Cii and 1Dii). However, silk with different initial conformations responds differently to the imprinting process but similarly to the deformation process. In amorphous silk, the majority of the molecular chains are activated for rearrangement due to the glass transition when interacting with water vapor, which causes the protein molecules to reflow for imprinting (Figure 1Ciii). In contrast, in crystalline silk, water molecules can only infiltrate the noncrystalline regions, resulting in local protein chain movement that is unable to reflow during imprinting due to the restriction from the crystalline domains (Figure 1Diii). Therefore, the imprinting process is feasible only on amorphous silk and not on crystalline silk. In the case of the water-vapor-induced shape-transformation process, as water molecules permeate from one surface of the film and progressively diffuse toward the opposing side, both amorphous and crystalline silk matrices generate a gradient distribution of water molecules along the thickness direction

(Figures 1Cii and 1Dii). The silk film, constrained by the PDMS substrate underneath, reaches a new planar equilibrium state even in the presence of a water molecular gradient, through continuous molecular rearrangement that induces the release of interfacial stress caused by the unbalanced swelling. As a consequence, upon the release from PDMS binding and subsequent water-molecule evaporation, the film spontaneously bends toward the vapor-exposed side to reach another new equilibrium state (Figures 1Civ and 1Div). As the duration of water-vapor fumigation increases, water molecules permeate the silk film to a greater extent, leading to an intensified concentration gradient. Accordingly, the complete elimination of water molecules would yield a more pronounced bending angle. It is important to note that the formation of the water molecular gradient is critical for the spontaneous deformation process, as we have observed that the film fails to deform after the gradient is eliminated under long-term vapor exposure. It should be noted that all protein matrices utilized in this study are based on amorphous silks unless otherwise specified.

The imprinting method utilized in this study can produce micro-/nanostructured silk films of various types (e.g., one-dimensional [1D] grating) over a large area, without the need for specific treatments such as solvent immersion, and can be performed under normal temperature and pressure (Figure 1E). Silk protein, used as the building material, ensures the master mold's replication with high fidelity and consistency throughout the embossed region due to its excellent characteristics, such as mechanical robustness, water-based manufacture, and multilevel processibility.[40,41] The outstanding optical transparency of silk film along with its high refractive index (Figure S3) guarantees that the optically imprinted microstructures fully showcase their optical functionality. Besides, the excellent adhesion property of silk protein enables the production of stable polyfunctional coatings on substrates of different textures and topographies. For example, silk films with a QR code pattern and a bilingual "Nanjing University" pattern can be firmly attached to the flat lid and curved body of a glass container, respectively (Figure 1F). Furthermore, 2D silk planar structures can be combined with sophisticated origami or kirigami techniques to create various complex 3D configurations, resulting in a wide range of multiplexed functions (Figures 1G and S4). These 2D/3D multifunctional platforms are optically and structurally stable under ambient conditions, making them suitable for various information display and encryption applications as demonstrated below. Moreover, the platforms can be optically rewritten and structurally reprogrammed by exploiting the reversible molecular rearrangement of silk protein induced by water vapor. This enables the erasure of the encoded optical micro-/nanostructures and 3D configurations, resetting the platforms to their original "blank" state for rewriting and reprogramming. Last but not least, the inherent environmental friendliness, biocompatibility, and biodegradability of silk protein[41,42] make the multifunctional optical platforms non-polluting to the environment and establish a favorable interface with the human body. The encoded film can be completely dissolved through water immersion after use, thanks to the water solubility of the silk matrix assembled in its amorphous state (Figure 1H).

Rewritable optical elements by micro-/nanoimprinting

The achievement of multiplexed functions relies on the rewritable patterned optical structures, which are fabricated through a water-vapor-induced local imprinting process utilizing shadow masks. As illustrated in Figure 2A, the process begins by exposing an amorphous silk film to water vapor through a shadow mask with a desired pattern, such as a butterfly shape. Following this, a grating master is adopted to conduct imprinting after removing the mask. The grating structures are only

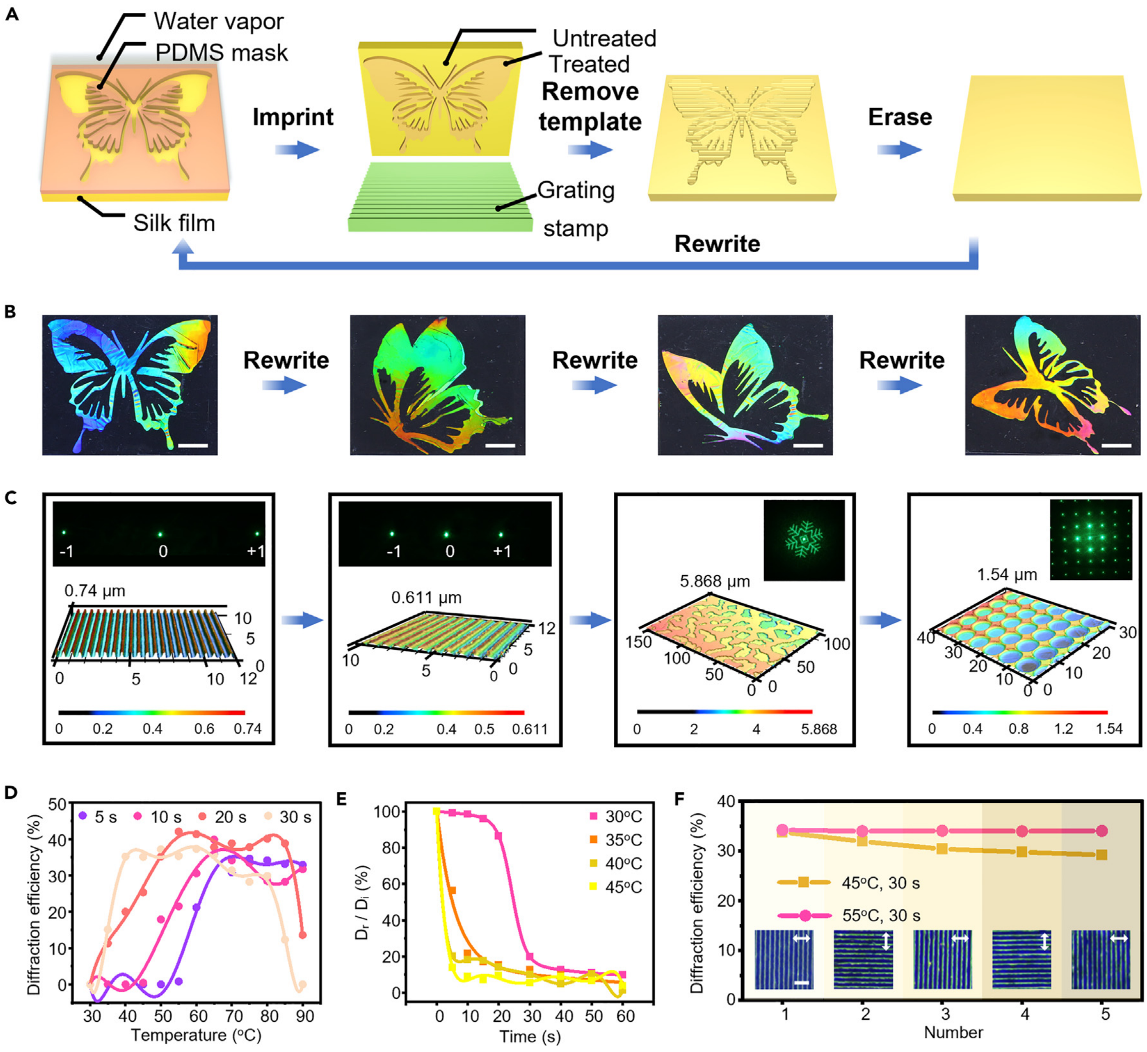

Figure 2. Rewriting of optical structures on silk films via water-vapor-enabled micro-/nanoimprinting

(A) Schematic of preparation and rewriting of patterned optical structures.

(B) Photographs showing the sequential generation of butterfly patterns with four different postures on a silk film. Scale bars, 5 mm.

(C) Laser scanning confocal microscopy images of different optical elements sequentially imprinted in the same area of a silk film. From left to right: a holographic grating with a rectangular cross-section (1,800 grooves/mm), a blazed grating with a triangular cross-section (1,200 grooves/mm), a diffractive optical element (DOE) with step structure, and a DOE with circular hole arrays. The insets present the corresponding diffraction patterns.

(D) Dependence of diffraction efficiency of a grating pattern (600 grooves/mm) on fumigation temperatures of water vapor.

(E) The ratio of residual diffraction efficiency (D_r) to the initial diffraction efficiency (D_i) as a function of erasure time in water vapor.

(F) The variation of diffraction efficiency of the imprinted grating during continuous direct rewriting. The nanoimprinting was performed alternatively vertically and horizontally to distinguish each rewritten process. The insets show corresponding microscopic images. Scale bar, 5 μm.

written in the exposed region, resulting in a butterfly pattern with vivid angular-dependent structural color. The imprinted optical structures can be erased via water-vapor-induced molecular chain movement, which restores the nanostructured surface to its flat state, allowing for the silk film to be reimprinted to produce a different pattern. This rewriting feature is demonstrated in Figure 2B, where four different poses of butterfly patterns are sequentially printed in the same area of a silk film. Each pattern displays a multispectral color range from blue to red, a phenomenon derived from the inherent angle dependence of grating structures. This effect can be mitigated by increasing the observing distance while maintaining a constant viewing angle. What is more, silk film can perform sequential imprinting with optical elements of various microstructures, from gratings of different periods to assorted diffractive optical elements (DOEs), as shown in Figure 2C (see also Figure S5). We found that the silk film demonstrates the capability to replicate nanostructures of dimensions less than 100 nm using the water-vapor-enabled imprinting method developed here (Figure S6).

The imprinted silk film can fully duplicate the microstructures of the corresponding master mold and reproduce their optical function (Figure S5; Tables S2 and S3). The success of achieving such a high level of fidelity in the imprinted constructs is attributed to the sufficient reflow of the "melted" silk protein, which can be regulated by controlling the fumigation temperature and exposure time of water vapor while maintaining a constant applied pressure during imprinting. We demonstrated this effect by examining the diffraction efficiency of the imprinted silk films generated through water-vapor exposure at varying temperatures for different durations. (Figure 2D). We found that films with longer processing times achieve maximum diffraction efficiency at lower temperatures. For instance, the sample treated for 30 s reaches the plateau of around 30% at 40°C while it requires up to 70°C for samples treated for 5 s. Increasing the water-vapor treatment temperature or time favors the movement of molecular chains and subsequent imprinting, enabling the duplication of the master pattern with better integrity. However, excessively high treatment temperatures, particularly for long-time exposure (such as 30 s), will cause conformational transitions in the silk protein (Figure S7), impeding the molecular rearrangement and decreasing the diffraction efficiency. Similarly, water-vapor treatment conditions also affect the erasing process. The increase in exposure temperature speeds up the erasure of the imprinted grating microstructures (Figure 2E). Owing to the structural stability of amorphous silk film under cyclic moisture absorption and desorption when using 45°C/55°C water vapor as a humidity source (Figure S8), it exhibits good endurance for repeated imprinting and erasing, with no significant deterioration in diffraction efficiency over five cycles (Figure 2F). Notably, the preservation of the stability of the imprinted microstructure (Figure S9 and Table S4) and the maintenance of diffraction efficiency in the serial imprinting scenario relies on the sufficient movement of the silk protein molecular chains during subsequent imprinting, since the previous imprinting inevitably compacts the protein chains. To further improve the imprinting performance, including imprinting fidelity, resolution, and cycle numbers, it is imperative to optimize the molecular composition of silk protein, ensuring a more uniform molecular weight and a stable, high-content amorphous conformation. Unless otherwise specified, both the imprinting and erasing processes were conducted by water-vapor treatment at 45°C for 30 s.

Complex dynamic display systems via multistep imprinting

The precise manipulation of water-vapor exposure in a spatiotemporal manner, together with the rewritable nature of imprinted microstructures, offers a reliable approach for creating complex and multispectral patterns through the spatial encoding of optical structures via a sequence of imprinting steps on one or both sides of a silk film. To showcase the broad range of optical functionalities that can be incorporated into a single silk-film platform, a series of imprinting strategies were devised and demonstrated.

The first strategy developed for constructing complex multispectral patterns involves the local rewriting of grating nanostructures with the aid of masters of different periods. As a demonstration, an iridescent Chinese character "Fu" pattern was fabricated, which stands out from the surrounding background at the same

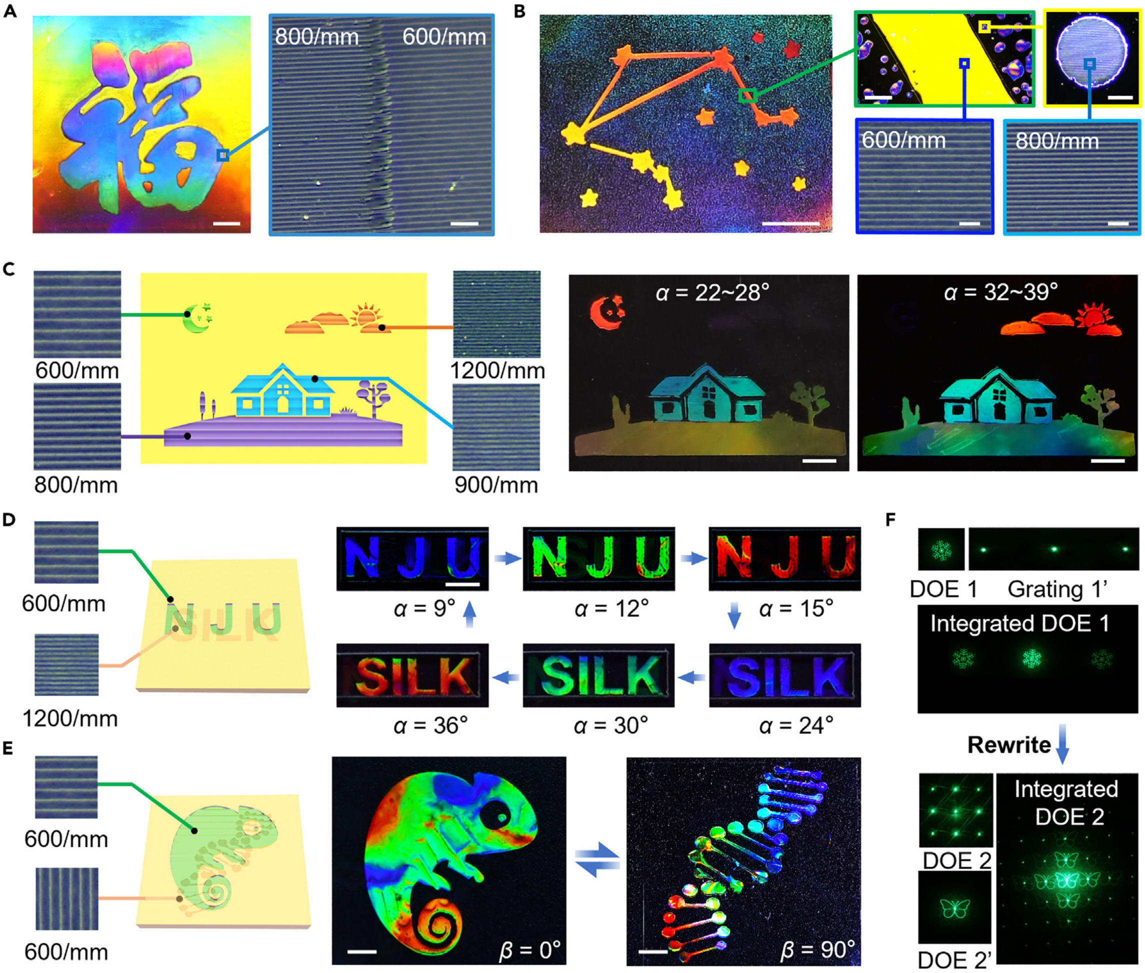

Figure 3. Engineering of complex, dynamic display systems through the integration of different optical elements

(A) Photograph showing the generation of a Chinese character "Fu." The microscopy image shows the seamless integration of two gratings. Scale bars, 5 mm (left) and 5 μm (right).

(B) Photographs of a starry sky highlighting libra stars patterned on the silk film, and corresponding microscopy images showing imprinted grating structures. Scale bars, 1 cm (left), 200 μm (right upper left), 20 μm (right upper right), and 5 μm (right lower).

(C) (Left) Schematic of the formation of a multicolor landscape painting and the corresponding microscope images. (Right) Corresponding photographs of the painting observed at different viewing angles (α). Scale bars, 5 mm.

(D and E) (Left) Schematics of angular-dependent dynamic structural color systems based on double-sided nanoimprinting of gratings: same orientation but different periods (D), and same period but orthogonal orientation (E). (Right) Corresponding photographs showing the letters change from "NJU" to "SILK" and the conversion from chameleon pattern to double-stranded DNA pattern with the increase of α and β, respectively. Scale bars, 5 mm.

(F) Diffraction patterns of rewritable, integrated DOEs based on the double-sided nanoimprinting of two different optical elements.

viewing angle (Figure 3A). Optical microscopy images show that the two different grating microstructures with parallel orientations are seamlessly integrated, thanks to the water-vapor-induced direct rewriting process. It is noteworthy that even after being stored at ambient conditions (20°C–30°C, 30%–60% relative humidity [RH]) in the lab for 12 months, this "Fu" pattern still maintains its initial conformation, morphology, and diffraction capabilities and can be effectively rewritten into a new pattern (Figures S10A–S10I), demonstrating the excellent stability of micro-/nanostructures and high performance in terms of rewriting of imprinted silk platforms. In addition, a starry-sky pattern with libra stars highlighted was imprinted on the silk film to demonstrate the complexity of achievable patterns (Figure 3B).

In this case, a background was first printed using "pixelated" imprinting through the exposure of the silk film to water mist rather than water vapor. The use of water mist enables the sporadic and random attachment of micrometer-sized droplets to the surface of the silk film, where the molecular chains become movable for imprinting. The libra stars were then patterned on by rewriting the film with a grating master of another period after exposing the film to water vapor through a customized mask. Enlarged images provide a clear view of the uniform and pixelated morphology within and outside of the rewritten area, respectively.

Imprinting gratings of different periods on different regions of the same silk-film surface serves as an efficient strategy for reversible pattern switching by changing the viewing angle. This approach exploits the fact that the spatial angle range of grating diffraction varies with the period (Figures S11 and S12). To demonstrate this capability, a landscape painting was created by imprinting patterns of the moon and stars, house, lawn, sun, and clouds on four different areas of the silk film, with each area using a different grating period (Figure 3C, left). Since there is no overlap of diffraction spectra between the gratings used to construct the moon and stars versus the sun and clouds patterns, a change in viewing angle α (Figure S13) from 22°–28° to 32°–39° causes a transition from a night view (with the moon and stars pattern visible) to a day view (with the sun and clouds pattern visible), and the house and lawn patterns remain visible throughout. This landscape pattern retains its initial color appearance and pattern-switching capability even after being stored at ambient conditions (20°C–30°C, 30%–60% RH) in the lab for 12 months (Figures S10J and S10K).

Furthermore, the aforementioned imprinting strategies can be extended to both sides of the silk film to further enhance and integrate the functionalities. By imprinting at the same position on both sides of the film, encoding structures can exhibit "parallel" and "cascade" functions. The former enables dynamic pattern switching by utilizing the spatial angle dependence of the grating structure (Figure S14),[43–45] realized by imprinting either two gratings of different periods in parallel alignment or two gratings of the same period in orthogonal orientation on the two sides of the silk substrate. To demonstrate this concept, a dual-patterned film displaying the patterns "NJU" and "SILK," featuring grating structures in the same orientation, was fabricated via double-sided imprinting. The "NJU" letters were patterned using a 600 grooves/mm grating, while the "SILK" letters were patterned using a 1,200 grooves/mm grating. As illustrated in Figure 3D, an increase in viewing angle (α) first causes the color of the "NJU" letters to shift from blue to red and then switches the observed pattern to the "SILK" letters, followed by a red shift in their color (Video S2). In another scenario, a chameleon pattern and a double-stranded DNA pattern, generated using a grating of the same period (600 grooves/mm), were orthogonally imprinted on the two sides of a silk film (Figure 3E). The transformation from the chameleon pattern to the double-stranded DNA pattern was observed when the central angle of the viewing direction (β) (Figure S13) changed from 0° to 90° (Video S3).

In addition, the "cascade" of two different types of optical elements on two sides of the film enables the generation of merged diffraction patterns, offering an efficient strategy for improving information storage capacity and the complexity of the output information. For example, when a grating and a DOE are cascaded, the diffraction pattern of the DOE (a snowflake used here) emerges at each diffraction order of the grating (Figure 3F). The robustness of the material allows for easy rewriting of micro-/nanostructures on both sides of the film, thus renewing the output multiplexed information.

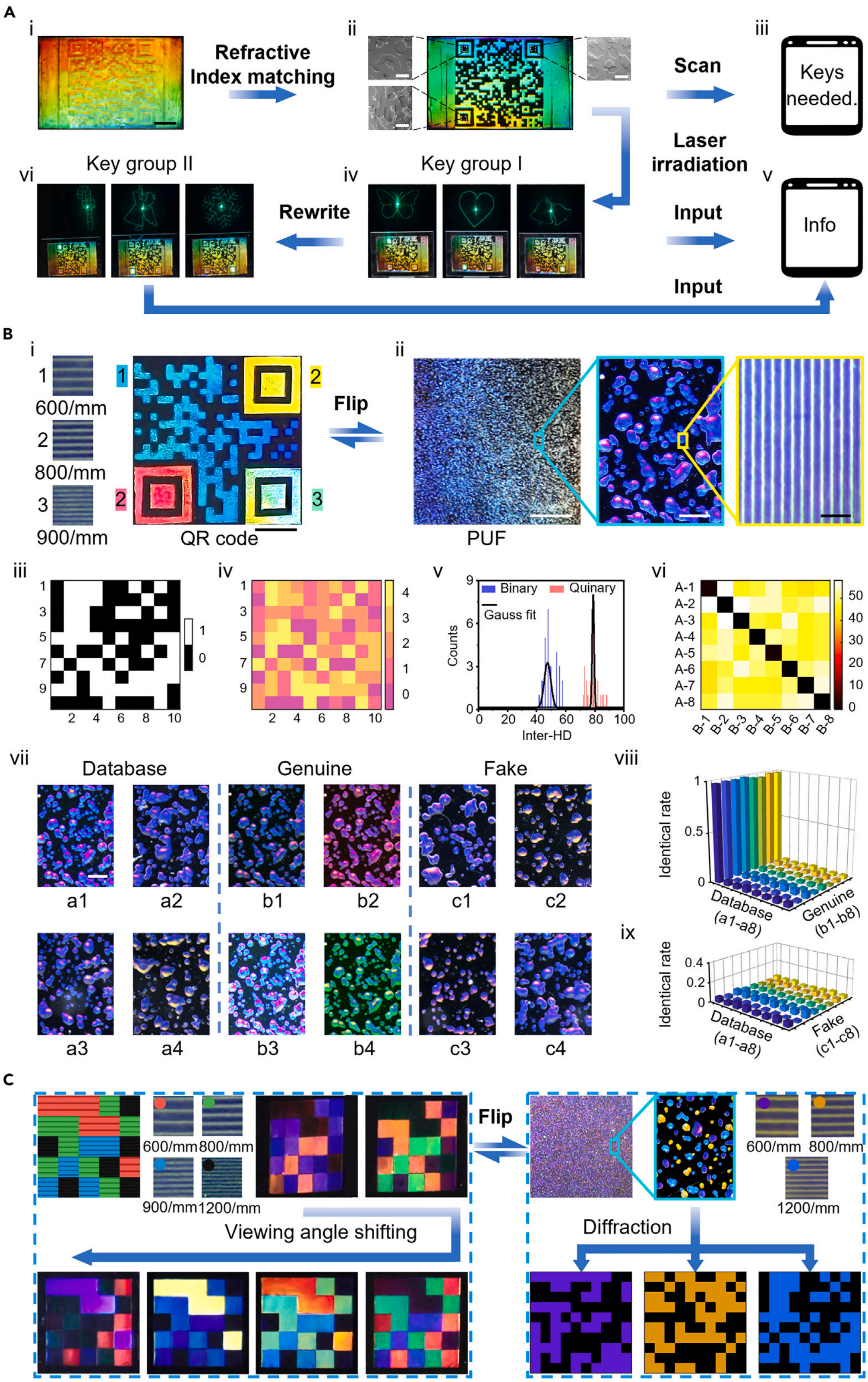
A
i
Refractive Index matching
ii
Scan
iii
Keys needed.
Laser irradiation
Key group II
vi
iv
Key group I
v
Rewrite
Input
Info
Input
B
i
1
600/mm
2
800/mm
3
900/mm
1
2
2
3
QR code
Flip
ii
PUF
iii
1
3
5
7
9
2 4 6 8 10
1
0
iv
1
3
5
7
9
2 4 6 8 10
4
3
2
1
0
v
Binary
Quinary
Gauss fit
Counts
9
6
3
0
0 20 40 60 80 100
Inter-HD
vi
A-1
A-2
A-3
A-4
A-5
A-6
A-7
A-8
B-1
B-2
B-3
B-4
B-5
B-6
B-7
B-8
50
40
30
20
10
0
vii
Database
Genuine
Fake
a1 a2 b1 b2 c1 c2
a3 a4 b3 b4 c3 c4
viii
Identical rate
1
0.5
0
Database (a1-a8)
Genuine (b1-b8)
ix
Identical rate
0.4
0.2
0
Database (a1-a8)
Fake (c1-c8)
C
600/mm
800/mm
900/mm
1200/mm
Flip
600/mm
800/mm
1200/mm
Viewing angle shifting
Diffraction

Figure 4. Use of versatile imprinted silk films for multistage and multilayer encryption

(A) Multistage encrypted QR code label. (i) Unrecognizable label. (ii) A clear QR code after refractive index matching. Scanning electron microscopy images exhibit the morphology of the imprinted DOEs within the three open squares of the QR code. (iii) Scanning result. (iv) Keys extraction. (v) The decrypted message. (vi) Rewriting of the keys. Scale bars, 5 mm (i) and 10 μm (ii).

(B) Multilayer anti-counterfeiting tag based on multicolor QR code and single-color PUF. (i) Photograph of the QR code. (ii) Photograph of the PUF. (iii) Binary code. (iv) Quinary code. (v) HD calculated among eight PUF samples. (vi) HD of twice-measurements of eight PUF samples with binary code. The x or y axis represents the first and second measurements, and the color bar indicates HD. (vii) Microscope images of label samples from the database (a1–a4), sample a1 taken with different factors (b1–b4), and fake label examples (c1–c4). (viii and ix) Identical rates of genuine samples (viii) and fake samples (ix). Scale bars, 5 mm (i, ii [left]), 200 μm (ii [middle], vii), 5 μm (ii [right]).

(C) Multilayer anti-counterfeiting tag based on 3D color code and tricolor PUF. (i) Schematic of the 3D color code and corresponding photographs taken at various viewing angles. (ii) Photograph of the tricolor PUF and corresponding binary code matrices separately processed from the diffraction optical power of the three imprinted gratings.

Multistage and multilayer encryption devices

The ability to encode various images in different channels and dynamically switch between them in multiple ways, combined with the capacity to redefine the imprinted optical structures and renew the outputted information, endows the multifunctional platforms with the potential for high-security-level anti-counterfeiting. Figure 4 illustrates three types of security labels that exhibit high-security levels through multistage and multilayer encryption, respectively.

QR codes have become a ubiquitous system for storing and accessing information, owing to their high storage capacity, error-correction capability, and ease of use. However, on some occasions it is undesirable to publicly display the information contained in a QR code after it is scanned. In this study, the presented multifunctional platform can endow QR codes with multistage encryption functionalities. As a proof of concept, we fabricated a dual-stage encrypted QR code by imprinting a grating-based QR code pattern on one side of a silk film and an unpatterned grating background with the same orientation and period on the other side before embedding different DOE microstructures into the three square areas of the QR code. As shown in Figure 4A, two steps are required to decipher the messages encoded in the label: (i–iii) retrieving the QR code by matching the refractive index of the background grating and (iv and v) accessing the key by extracting the diffraction patterns of the imprinted DOEs. At first the QR code on the prepared label is unrecognizable, but it is revealed once the background side of the label is attached to an oxidized PDMS substrate, which eliminates the interference of the background grating (Figures 4Ai and 4Aii, 1st encryption stage). This step enables the scanning by a smartphone (Figure 4Aiii). The diffraction patterns within the three squares can be read out by irradiating the regions with a laser pointer, from which the key to the 2nd encryption stage is extracted (Figure 4Aiv and Video S4). After inputting the names of diffraction patterns, the message contained in the QR code is finally acquired (Figure 4Av). Evidently, the key can be updated by rewriting another set of DOE microstructures into the three squares, thereby reducing the risk of key leakage.

Although the multistage encrypted QR code can enhance information security by increasing decryption difficulty, it remains vulnerable to forgery in real-world applications. As an alternative, Physical unclonable functions (PUFs) have emerged as one of the most effective anti-counterfeiting strategies due to their intrinsic stochastic, unpredictable, and non-replicable physical features.[46–48] The "pixelated" imprinting method described in this work enables the incorporation of PUF into anti-counterfeiting labels. To demonstrate this concept, we fabricated a security label with triple-layer encryption capabilities by integrating orthogonally oriented multicolor QR code and PUF on both sides of a silk film. The three encryption layers leverage different signals, namely multicolor QR code signals, far-field diffraction signals, and color image signals. In the first encryption layer, a multicolor QR code generated by local imprinting using gratings of different periods as the masters allows rapid authentication using a smartphone, within which the added color information raises the difficulty of counterfeiting (Figure 4Bi). The PUF label featuring randomly distributed grating islands fabricated using water-mist-induced imprinting can be verified through diffraction signal extraction as well as direct image recognition, representing the second and third encryption layers, respectively (Figure 4Bii).

As the name suggests, the PUF operates as a single-valued function, whereby the input signal (known as "Challenge") interacts with the PUF entity and produces a corresponding signal ("Response"), which is referred to as a challenge-response pair.[47,49] To implement the second layer of encryption, the PUF label was divided into a 10 × 10 pixel matrix and scanned pixel by pixel with a laser pointer. The optical intensity of the first diffraction order was measured by an optical power meter, serving as the response. Notably, the optical diffraction of the QR code does not affect the extraction of the optical intensity signal of PUF because of their mutually perpendicular grating orientation. The optical intensity of the diffraction beam depends on the density of the imprints in the pixel region, with denser imprinted domains producing stronger measured optical intensity. An appropriate and adaptive threshold value was determined by the algorithm, and pixels with light intensity exceeding the threshold were assigned as 1-bit while those below were assigned as 0-bit. According to this procedure, a 100-bit binary serial number enclosed in the security label was extracted, which could be used to authenticate the products (Figure 4Biii). Additionally, the pixel matrix could be further subjected to quinary processing by setting four threshold values (Figure 4Biv), increasing the label's capacity from 2^{100} to 5^{100}.

To assess the performance of the as-prepared PUF labels, three key indicators were evaluated.[47] The first indicator is bit uniformity, which represents the degree of randomness of the bit distribution in the binarized pixel matrix and can be calculated from the following equation:

$$\text{Bit uniformity } = \frac{1}{n}\sum_{i=1}^{n} P_i, \qquad \text{(Equation 1)}$$

where P_i is the i^{th} bit of the binarized pixel matrix with n bits. Since each pixel has a half possibility of being 0 bit or 1 bit, the ideal value of the bit uniformity is 0.5. For eight different PUF labels, the calculated bit uniformity is exactly the ideal value, indicating a high degree of randomness due to the selection of adaptive threshold values (see experimental procedures for details). The second indicator is label uniqueness, which reflects the degree of difference between different PUF labels and is calculated by inter-label hamming distance (HD):

$$\text{Label uniqueness} = \frac{2}{N(N-1)}\sum_{i=1}^{N-1}\sum_{j=i+1}^{N}\frac{\text{HD}(P_i, P_j)}{M}, \qquad \text{(Equation 2)}$$

where P_i and P_j are M-bit keys of the i^{th} PUF label and the j^{th} PUF label among N different PUFs, respectively. The pairwise comparison results of the inter-label HDs of the eight binarized and quinarized samples are shown in Figure 4Bv, and the calculated average inter-label HD of binary codes is 49.9287, which is close to the ideal value of 50, indicating a high level of differentiation between different PUF labels. The last indicator is readout reproducibility, which refers to the consistency of the PUF label's output tested at multiple time points. Only when testing the label at different times leads to highly consistent results can the PUF label's reliability be secured. For the i^{th} PUF label, it is calculated from the average intra-label HD:

$$\text{Readout reproducibility} = \frac{1}{T}\sum_{t=1}^{T}\frac{HD(P_i, P_{i,t})}{n}, \qquad \text{(Equation 3)}$$

where P_i is the original n-bit key and $P_{i,t}$ is the same pixel matrix tested at another time point t, T is the number of repeated tests. As shown in Figure 4Bvi, the horizontal and vertical axes represent the first and second binary test results of eight labels, respectively (the quinary result is shown in Figure S15). The values on the diagonal line represent the HD between the same PUF label and are much smaller than the off-diagonal values, which represent HD between different PUF labels. These results demonstrate the excellent uniqueness of the PUF labels, allowing them to be recognized with high accuracy. Moreover, the PUF labels exhibit long-term reliability (2 months) under the same challenges in the ambient environment (20°C–30°C, 30%–60% RH) (Figure S16). Furthermore, the exceptional stability exhibited by the imprinted silk film across a range of environmental conditions (Figure S17) would significantly broaden the potential application contexts for the PUF labels.

In addition, the inherent randomness of the morphology and distribution of the grating islands can be leveraged as another layer of encryption (third encryption layer) for anti-counterfeiting purposes. In this scenario, an artificial intelligence (AI) technique that performs well in direct image recognition is employed to determine the authenticity of the PUF labels from microscope images.[50,51] The identification process consists of two steps: database establishment and matching calculation.

In the first step, the features of optical microscope images of genuine PUF labels were extracted using in-house algorithms and stored in a database for subsequent image recognition. Figures 4Bvii and S18 show three groups of eight label sizes, where a1–a8 represent genuine labels, b1–b8 represent label a1 captured under different imaging conditions (exposure time, brightness, contrast, hue, or arbitrary mix of these parameters), and c1–c8 are examples of fake labels that are not included in the database. To evaluate the performance of AI image-recognition algorithms, b1–b8 and c1–c8 were sequentially fed into the system and matched with all samples inside the database. Results indicate that b1–b8 have high similarity (over 95%) with a1 but low similarity with a2–a8, and reasonably all of them are identified as label a1 (Figure 4Bviii). Conversely, c1–c8 have low similarity (<5%) with every sample inside the database and are therefore identified as fake labels (Figure 4Bix). We also demonstrate the practicality of our approach by presenting the verification processes of a genuine label and a fake label based on a 100-sample-size database (Video S5).

To further improve information capacity and encryption level, we created another security label with triple-layer encryption capabilities by replacing the 2D code with a 3D color code and transforming the single-color PUF into a three-color PUF. A 3D color code is developed from traditional black-and-white 2D code and can store additional information to confer a higher level of security due to its composition of different color matrices.[52,53] Taking advantage of color variations exhibited by gratings of varying periods, a 3D color code could be generated on a silk film through the localized impression of gratings of different periods (Figure 4Ci). This 3D color code demonstrates an angle-dependent color presentation, and the readable 3D color code (marked with a red border) can exclusively be extracted from a specific viewing angle ($\alpha = 0°$). The inclusion of unreadable information states contributes to a heightened level of encryption. Meanwhile, a three-color PUF label created through successive imprinting of three distinct periods of gratings onto water-mist-treated silk film shows improved extracted bitstream capacities (from 2^{100} to 3×2^{100} for binary code and from 5^{100} to 3×5^{100} for quinary code) and offers richer information for image recognition (Figure 4Cii) in comparison with a single-color PUF label. These results demonstrate the capacity of multifunctional platforms to achieve high-security encryption with high storage capacity through simple and cost-effective processing techniques.

3D information display and encryption devices

The spatial-controllable and multi-strategy imprinting technique enables the integration of multiple mutually independent pieces of information, allowing for multichannel and multimode imaging. However, transforming 2D encoded structures into 3D platforms provides an additional spatial degree of freedom in information encoding and multiplexing. Silk films, with their controllable deformability into complex and multimodal 3D configurations using water-vapor-enabled origami or kirigami technology (Figure 1G), permit this capability. By extending the encoded information from a 2D plane to a desired 3D space, 3D-geometry-controlled information integration becomes possible. Moreover, the stability exhibited by the silk film during cyclic deformation (Figures S19 and S20) enables the reprogramming of shape morphing, leading to the formation of switchable 3D architectures (Figure S21). This capability, combined with the rewritability of the imprinted optical structures, provides appended functionality for information renewal and substitution in 3D multiplexing devices. These features are demonstrated through the utility of the morphed platform for 3D multidirectional display and high-level encryption.

To demonstrate the potential of the 3D platform for multiplexing image display, a 3D dual-mode display device that integrates multifaceted color display and multidirectional holography was fabricated (Figure 1B). The device consists of a cube-shaped architecture, wherein the initials "T," "D," "F," "B," "L," and "R" of "Top," "Down," "Front," "Back," "Left," and "Right" were written on each facet of one side of its 2D precursor using gratings of different periods via the local rewriting method (Figure 5Ai). The orientations of grating structures within and outside of the letter area on each facet are arranged to ensure that the erect image of each letter can be observed separately after folding (Figures 5Ai and 5Aii). Next, a grating and five DOEs with different diffraction signals were locally imprinted on each facet of another side of the precursor, with the orientation of the grating being perpendicular to that of the grating on the letter side (Figures 5Av and 5Avi). After folding the encoded 2D precursor into a box, the 3D dual-mode display can be achieved by manipulating the light illumination mode, direction, and wavelength. Under white-light illumination in reflection mode, the device can individually display the colorful letter pattern encoded on each facet in a specific irradiation direction or simultaneously display two or more letters when illuminated in multiple directions (Figures 5Av and 5Avi). However, when illuminated vertically from the facet with orthogonally oriented gratings using a green laser, the device yields five different holographic images of a heart, bell, snowflake, butterfly, and genie simultaneously in far-field in different spatial directions (Figure 5Avii). The multiplexing of five holographic images is achieved by utilizing the zero-order and four first-order diffraction beams generated from the orthogonally oriented gratings as light sources to shoot the DOEs imprinted on the other five facets (Figure 1B). The output image information of this 3D device can be refreshed by means of shape reconfiguration and imprint rewriting. For instance, another five DOEs can be embedded to obtain a new set of holographic images (Figures 5Avi and 5Avii). Overall, the introduction

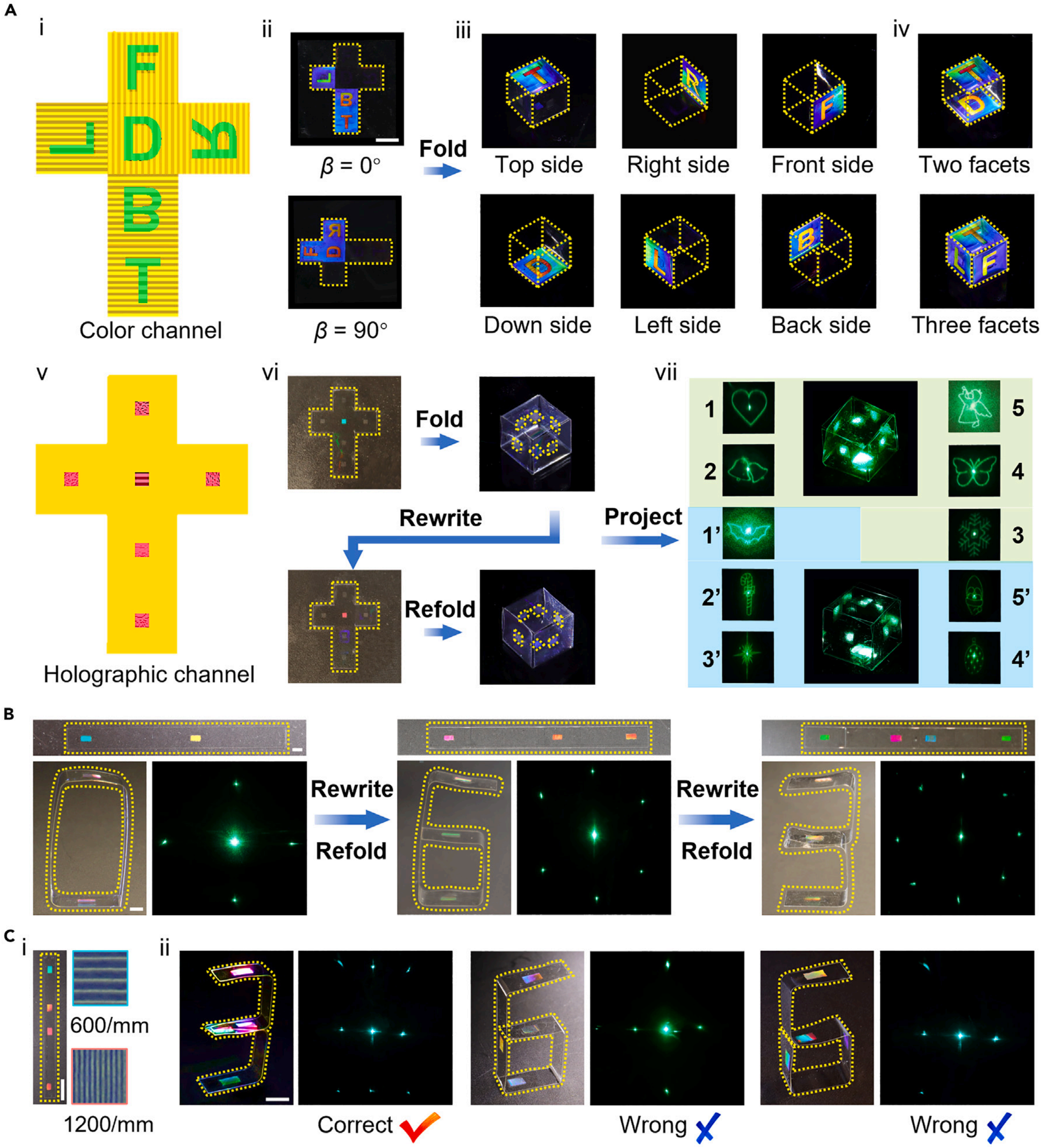

Figure 5. 3D multidirectional display and high-level encryption devices

(A) Schematics and photographs demonstrating the integration of multifaceted color images and multidirectional holographic images within a single cube-shaped device. (i) Schematic of the 2D precursor showing the structural color channel. (ii) Photographs of the corresponding 2D precursor at two orthogonal viewing angles. (iii) Photographs of the folded box that shows the printed letter in each facet individually. (iv) Photographs of the folded box showing the printed letters in two and three facets simultaneously. (v) Schematic of the 2D precursor showing the holographic channel. (vi) Photographs of the 2D precursor and folded box with locally imprinted, rewritable optical structure in each facet. (vii) Corresponding photographs of the cubes (before and after reprogramming) during laser irradiation and the projected diffraction patterns. Scale bar, 1 cm.

(B) The recording and formation of an integrated diffraction pattern through the programmed combination of a rewritable 2D grating structure and a reconfigurable 3D configuration. Scale bars, 2 mm.

(C) 3D information encryption based on reprogrammable architectures. (i) Photograph of a patterned silk strip and microscope images of the imprinted gratings. (ii) Decryption of information through specific folding and proper irradiation. Scale bars, 5 mm.

of 3D architectures offers several advantages over 2D planes for image display and transition. Specifically, the formation of a 3D spatial architecture allows the capability to switch between multiple distinct color images (>6) within one single device as the incident or viewing angle changes. Additionally, the implementation of a 3D architecture increases the display and perception dimension (Figure S22). This enables the presentation of images from various directions within 3D space or the capture of color images from multiple 3D perspectives, leading to enhanced spatial perception and the ability to switch viewpoints in 3D space. Moreover, the 3D configuration offers the capability to simultaneously display multiple holographic images in 3D space while utilizing a single light source for excitation, opening up new possibilities for advanced holographic imaging.

The combination of reprogrammable 3D configurations and rewritable 2D diffraction structures highly increases the freedom of functional integration, especially when it comes to the fusion of far-field diffraction signals. To demonstrate this, we designed different diffraction patterns by rationally combining the grating structures and 3D shapes. As shown in Figure 5B, diffraction patterns with four, six, and eight first-order diffraction signals can be generated successively using one silk strip (60 mm × 5 mm × 50 μm) by rearranging the distributions and orientations of grating structures (for details see experimental procedures) while reprogramming its 3D structures from "0" to "6" and then to "3".

The spatial order introduced by the 3D configuration can be further exploited alone to design diffraction patterns. Different 3D shapes derived from the same 2D precursor output significantly different diffraction patterns, which makes the 3D device promising for information encryption. As a proof of concept, we fabricated a silk strip printed with specially designed grating structures (Figure 5Ci). The encrypted information is not discernible when the strip is in its flat state. To reveal the information, a morphing process must be carried out, and only when the strip is deformed into the specified shape and illuminated appropriately can the correct information be retrieved. As shown in Figure 5Cii, folding the strip into the shape of a number "3" and illuminating it vertically from the 600 grooves/mm grating side with a green laser generates the correct information of the number "8" (Figure S23A). However, folding the strip into any other configurations, such as "6" shapes according to different folding methods and orders, would produce incorrect information (Figure 5Cii). Shooting the laser beam from the opposite direction would also lead to an incorrect message (Figures S23B and S23C). Notably, it is difficult to guarantee that the bend angle will be exactly the same every time, yet the same diffraction results can be secured because the microstructures are imprinted in an area rather than at a single point (Figure S24). These results suggest that correct cryptographic information can only be obtained when the encoded gratings form a specific spatial arrangement. By increasing the encoding complexity through meticulous engineering of both the imprinting and morphing processes, more intricate combined diffraction patterns (encrypted information) can be designed, leading to a higher level of information security. It is worth noting that the stability of the 3D architecture formed by folding the silk film is indeed an important consideration for the extraction of the desired diffraction information, and this stability concern can be further enhanced by increasing the thickness of the silk film. While it is true that the stability of the 3D architecture may decrease compared to its initial state, the exceptional mechanical properties of silk contribute to maintaining sufficient stability for the intended optical functionality. Furthermore, the repetitive deformation performance of the silk 2D precursors will influence the reproduction/update of the optical functionality determined by the 3D shape, which can be further improved by locally optimizing the assembly of silk protein structures, such as introducing physical/chemical crosslinking networks, to impart higher stability in response to water vapor.

DISCUSSION

The integration of protein self-assembly, 2D micro-/nanoimprinting, and 3D morphing techniques represents a powerful and efficient approach for creating protein-based multifunctional optical imaging platforms with reprogrammable architectures, geometries, and functions. The use of silk protein's desirable material properties, in combination with the spatial-controllable and multi-strategy imprinting technique, enables a simple yet versatile solution for multimode image switching, multistage encryption, and multilayer anti-counterfeiting. Additionally, the 2D multiplexing platforms support the development of 3D multidirectional imaging and high-level encryption devices, thanks to their capacity for multimodal and complex shape changes. The platform's ability to allow angular-dependent image switching in both 2D and 3D geometries, along with the availability of an optically/magnetically functionalized silk format for reversible, tunable, and adaptive actuation,[54,55] offers exciting possibilities for generating remotely controlled dynamic display systems by rationally integrating multiplexed optical functions and actuation in a single system. The multiplexing strategy presented here, along with the ease of functionalization of silk matrix, paves the way for multidimensional and high-security 2D/3D information encryption and anti-counterfeiting by embedding additional channels of concealable photochemical information such as fluorescent or phosphorescent signals into a versatile protein format. The biocompatible traits of these platforms suggest their applicability in bio-related scenarios, such as security labels on editable products or wearable smart display devices. Taking into account the inherent advantages of the imprinting technique, including high throughput, cost-effectiveness, and repeatability, these all-protein-based multifunctional optical imaging platforms exhibit significant potential for practical applications with the advancements in the large-scale production of silk materials and the optimization of the ''structure-property-function'' relationship of silk optical systems. The combination of versatile and variable protein formats, 2D diffraction optics, and 3D architectures opens up new avenues for the development of advanced and green optical information storage, encryption, anti-counterfeiting, and stereoscopic 3D display devices in the future.

EXPERIMENTAL PROCEDURES

Resource availability

Lead contact

Further information and requests for resources and reagents should be directed to and will be fulfilled by the lead contact, Yu Wang (yuwang87@nju.edu.cn).

Materials availability

This study did not generate new unique reagents.

Data and code availability

The data generated during this study are available from the corresponding author upon reasonable request.

Preparation of regenerated silk fibroin solution

Regenerated silk fibroin solution was extracted from the silk cocoons of the *Bombyx mori* silkworm using established protocols.[56] In brief, cocoon pieces were boiled in a 0.02 M Na_2CO_3 solution for 30 min and rinsed with deionized water to remove the hydrophilic sericin layer. After drying under ambient air for 2 days, the degummed silk fibers were dissolved in 9.3 M LiBr solution at 60°C for 4 h and subsequently dialyzed against deionized water for 3 days. The post-dialysis solution was centrifuged at 11,000 rpm for 20 min and filtered with air-laid paper to obtain a 6–7 wt % silk fibroin solution in water. The solution, when preserved in a 4°C refrigerator, would stay in its original state for at least 2 months.

Preparation of silk fibroin film

A cast film of amorphous silk with a thickness of approximately 50 μm was prepared by casting a certain volume of silk solution onto a silicon wafer treated with trichloro(1H,1H,2H,2H-perfluorooctyl)silane and drying at ambient conditions overnight. The crystalline silk film was generated after immersion in methanol for 30 min.

Micro-/nanoimprinting

Micro-/nanoimprinting of silk films was performed via a modified approach using the previously reported method.[37] First, an amorphous silk film was firmly attached to a clean PDMS substrate and exposed to water vapor at 45°C for 30 s (unless otherwise specified). The water vapor was generated using an enclosed thermostatic water bath device (NK-420; Nuoji Instrument), where the temperature and the amount of water vapor can be precisely set and maintained. When the chamber was filled with water vapor and reached equilibrium, the sample was quickly placed into the water vapor with the silk film side facing upwards. Next, once removed from the water bath, an optical element master featuring gratings of various periods or DOEs of different patterns was placed onto the surface of the wetted film and subjected to constant pressure. Following the drying and removal of the master, a silk film with micro-/nanostructured optical surfaces was obtained. The drying process comprises two steps: first, the partial evaporation of water vapor triggers the transition of the silk film from a flowing state to a glassy state; subsequently, following the detachment of the imprinted sample from the master, further evaporation of water vapor decreases its moisture content to ambient levels. To erase the imprinted patterns, the processed silk film was again exposed to water vapor at 45°C for 20 s. In the case of "pixelated" imprinting, one side of a silk film was exposed to water mist generated by a humidifier (buresBE-J001; Bures) at room temperature for 5 s. During the process, the distance between the sample and the mouth of the water-mist source is set as 20 cm, and the amount of water deposited on silk film increases with the prolongation of exposure time while maintaining a consistent distance and an equal amount of water-mist production (Figure S25).

Physical unclonable function label authentication

For the signal extraction type of verification, the label was fixed on an X-Z displacement stage (PT-SD412; PDV Instruments, China), which allowed for movement both vertically and horizontally. A laser pointer (2802; deli, China) with a diameter of 2 mm and a wavelength range of 500–552 nm was used as the excitation light source. The label was scanned point by point with a vertically incident laser beam by moving the stage at a step length of 2 mm. An optical power meter (PM100D; Thorlabs, USA) with a photodiode power sensor (S120VC; Thorlabs) was used to measure the first-order diffraction signal. The optical intensity of the first-order diffraction beam at every point in a 10 × 10 matrix was collected and input into a homemade MATLAB version.2022a program. The program used a global algorithm to determine an appropriate threshold value to binarize the matrix or four threshold values to quinarize the matrix. The program then evaluated the performance of the as-prepared PUFs, including their uniformity, uniqueness, and readout reproducibility, by calculating and visualizing their inter-HD and intra-HD. For AI verification, another homemade MATLAB program was designed. The PUF images were captured by optical microscopy and stored in the form of RGB values of 3,000 × 3,000 pixels. The MATLAB program transformed the input images to 1D grayscale, binarized them, and stored the result in the database. A pending PUF was processed according to the same process, and the resulting binarization/quinarization matrix was compared to each matrix in the database. The ratio of the number of pixels with the same value to the total number of pixels is regarded as similarity. A PUF label is considered genuine if its similarity value is higher than 90%.

Shape-morphing process

To fabricate micro-/nanostructured silk films of various 2D shapes, a commercial CO_2 laser cutter (SIR-2075; Trotec) was employed with a laser power intensity set to 6% of the maximum energy and a fixed speed of 1 step s^{-1}. To generate uniform shaping, a 2D silk film was rolled onto a glass rod with the micro-/nanostructured surface facing inward and exposed to water vapor for 1 min. After drying and detaching from the rod, a 3D-shaped sample was obtained. In cases where origami/kirigami-guided morphing was desired (e.g., Figure S26), a PDMS mask was first applied to a silk film that was affixed to a clean PDMS substrate, followed by local exposure to water vapor for 30 s (unless otherwise specified). Upon removal of the mask and detachment from the substrate, the sample automatically morphed into the targeted 3D structure. To erase the 3D architecture, the morphed silk film was flattened and secured onto a PDMS substrate by force and fumigated again with water vapor at 45°C for 30 s, during which time the imprinted patterns were safeguarded from interference.

Structural and properties characterization

Optical microscopy images were captured using an optical microscope (DM 2700M; Leica). The surface morphologies of imprinted silk films were observed with a field-emission scanning electron microscope (S-8100; Hitachi, Japan) at a voltage of 5 kV and a current of 10 μA. The 3D topographies of imprinted micro-/nanostructures were analyzed using a 3D laser scanning confocal microscopy (VKX1000; Keyence, USA). The silk protein conformational change after water vapor treatment was evaluated using a Fourier transform infrared absorption spectroscopy (FTIR) spectrometer (Nicolet IS50; Thermo Fisher Scientific, USA). All the FTIR spectra were acquired at a resolution of 4 cm^{-1} and an average of 16 scans in the range of 4,000–400 cm^{-1}. The transmittance spectrum was recorded using a fiber-optic spectrometer (PG2000-Pro; Ideaoptics Technology, China). The diffraction spectra of imprinted grating patterns were collected using an angle-resolved spectrometer (R1; Ideaoptics Technology, China) in transmission mode with a recording pre 1°. Diffracted patterns were obtained by propagating a green laser (2802; deli, China) with a wavelength range of 500–552 nm or a focused white light through the imprinted silk films. The distance between the sample and the projection plane was set at approximately 10 cm. Photographs and videos were taken with a digital single-lens reflex camera (EOS 850D; Canon).

SUPPLEMENTAL INFORMATION

Supplemental information can be found online at https://doi.org/10.1016/j.matt.2024.01.030.

ACKNOWLEDGMENTS

This work was supported by the National Key Research and Development Program of China (no. 2021YFA1202000), the National Natural Science Foundation of China (no. 62175102), the Natural Science Foundation of Jiangsu Province, Major Project (no. BK20212004), the Program for Innovative Talents and Entrepreneurs in Jiangsu (no. JSSCTD202138), and the Start-up Fund at Nanjing University (no. 14912226).

Also, many thanks to Prof. Desheng Kong at the College of Engineering and Applied Sciences, Nanjing University for his assistance with 3D laser scanning confocal imaging.

AUTHOR CONTRIBUTIONS

Y.W. and C.J. conceived the idea and designed the research. C.J., T.W., and Y.F. performed the research. All authors contributed to data analysis. Y.W., Y.L., and C.J. wrote the manuscript. Y.W. and Y.L. supervised the research.

DECLARATION OF INTERESTS

The authors declare no competing interests.

Received: October 27, 2023
Revised: December 26, 2023
Accepted: January 24, 2024
Published: February 20, 2024

REFERENCES

1. Lu, Y., Zhao, J., Zhang, R., Liu, Y., Liu, D., Goldys, E.M., Yang, X., Xi, P., Sunna, A., Lu, J., et al. (2014). Tunable lifetime multiplexing using luminescent nanocrystals. Nat. Photonics *8*, 32–36. https://doi.org/10.1038/nphoton.2013.322.
2. Chen, S., Liu, W., Li, Z., Cheng, H., and Tian, J. (2020). Metasurface-empowered optical multiplexing and multifunction. Adv. Mater. *32*, 1805912. https://doi.org/10.1002/adma.201805912.
3. Oh, J., Baek, D., Lee, T.K., Kang, D., Hwang, H., Go, E.M., Jeon, I., You, Y., Son, C., Kim, D., et al. (2021). Dynamic multimodal holograms of conjugated organogels via dithering mask lithography. Nat. Mater. *20*, 385–394. https://doi.org/10.1038/s41563-020-00866-4.
4. Dorrah, A.H., and Capasso, F. (2022). Tunable structured light with flat optics. Science *376*, eabi6860. https://doi.org/10.1126/science.abi6860.
5. Guo, X., Zhong, J., Li, B., Qi, S., Li, Y., Li, P., Wen, D., Liu, S., Wei, B., and Zhao, J. (2022). Full-color holographic display and encryption with full-polarization degree of freedom. Adv. Mater. *34*, 2103192. https://doi.org/10.1002/adma.202103192.
6. Zheng, Z., Hu, H., Zhang, Z., Liu, B., Li, M., Qu, D.-H., Tian, H., Zhu, W.-H., and Feringa, B.L. (2022). Digital photoprogramming of liquid-crystal superstructures featuring intrinsic chiral photoswitches. Nat. Photonics *16*, 226–234. https://doi.org/10.1038/s41566-022-00957-5.
7. Zijlstra, P., Chon, J.W.M., and Gu, M. (2009). Five-dimensional optical recording mediated by surface plasmons in gold nanorods. Nature *459*, 410–413. https://doi.org/10.1038/nature08053.
8. Lin, G., Baker, M.A., Hong, M., and Jin, D. (2018). The quest for optical multiplexing in bio-discoveries. Chem *4*, 997–1021. https://doi.org/10.1016/j.chempr.2018.01.009.
9. Du, K., Barkaoui, H., Zhang, X., Jin, L., Song, Q., and Xiao, S. (2022). Optical metasurfaces towards multifunctionality and tunability. Nanophotonics *11*, 1761–1781. https://doi.org/10.1515/nanoph-2021-0684.
10. Wei, Q., Sain, B., Wang, Y., Reineke, B., Li, X., Huang, L., and Zentgraf, T. (2019). Simultaneous spectral and spatial modulation for color printing and holography using all-dielectric metasurfaces. Nano Lett. *19*, 8964–8971. https://doi.org/10.1021/acs.nanolett.9b03957.
11. Lim, K.T.P., Liu, H., Liu, Y., and Yang, J.K.W. (2019). Holographic colour prints for enhanced optical security by combined phase and amplitude control. Nat. Commun. *10*, 25. https://doi.org/10.1038/s41467-018-07808-4.
12. Qu, G., Yang, W., Song, Q., Liu, Y., Qiu, C.-W., Han, J., Tsai, D.-P., and Xiao, S. (2020). Reprogrammable meta-hologram for optical encryption. Nat. Commun. *11*, 5484. https://doi.org/10.1038/s41467-020-19312-9.
13. Xiong, B., Xu, Y., Wang, J., Li, L., Deng, L., Cheng, F., Peng, R.W., Wang, M., and Liu, Y. (2021). Realizing colorful holographic mimicry by metasurfaces. Adv. Mater. *33*, 2005864. https://doi.org/10.1002/adma.202005864.
14. Kim, I., Jang, J., Kim, G., Lee, J., Badloe, T., Mun, J., and Rho, J. (2021). Pixelated bifunctional metasurface-driven dynamic vectorial holographic color prints for photonic security platform. Nat. Commun. *12*, 3614. https://doi.org/10.1038/s41467-021-23814-5.
15. Yang, W., Qu, G., Lai, F., Liu, Y., Ji, Z., Xu, Y., Song, Q., Han, J., and Xiao, S. (2021). Dynamic bifunctional metasurfaces for holography and color display. Adv. Mater. *33*, 2101258. https://doi.org/10.1002/adma.202101258.
16. Guo, X., Li, P., Zhong, J., Wen, D., Wei, B., Liu, S., Qi, S., and Zhao, J. (2022). Stokes meta-hologram toward optical cryptography. Nat. Commun. *13*, 6687. https://doi.org/10.1038/s41467-022-34542-9.
17. Fu, P., Ni, P.N., Wu, B., Pei, X.Z., Wang, Q.H., Chen, P.P., Xu, C., Kan, Q., Chu, W.G., and Xie, Y.Y. (2023). Metasurface Enabled On-Chip Generation and Manipulation of Vector Beams from Vertical Cavity Surface-Emitting Lasers. Adv. Mater. *35*, 2204286. https://doi.org/10.1002/adma.202204286.
18. Ko, B., Badloe, T., Yang, Y., Park, J., Kim, J., Jeong, H., Jung, C., and Rho, J. (2022). Tunable metasurfaces via the humidity responsive swelling of single-step imprinted polyvinyl alcohol nanostructures. Nat. Commun. *13*, 6256. https://doi.org/10.1038/s41467-022-32987-6.
19. Su, G., Li, Z., Gong, J., Zhang, R., Dai, R., Deng, Y., and Tang, B.Z. (2022). Information-Storage Expansion Enabled by a Resilient Aggregation-Induced-Emission-Active Nanocomposite Hydrogel. Adv. Mater. *34*, 2207212. https://doi.org/10.1002/adma.202207212.
20. Yao, X., Ma, H., Wang, X., Wang, H., Wang, Q., Zou, X., Song, Z., Jia, W., Li, Y., Mao, Y., et al. (2022). Ultralong organic phosphorescence from isolated molecules with repulsive interactions for multifunctional applications. Nat. Commun. *13*, 4890. https://doi.org/10.1038/s41467-022-32029-1.
21. Yang, Y., Liang, Y., Zheng, Y., Li, J.A., Wu, S., Zhang, H., Huang, T., Luo, S., Liu, C., Shi, G., et al. (2022). Efficient and color-tunable dual-mode afterglow from large-area and flexible polymer-based transparent films for anti-counterfeiting and information encryption. Angew. Chem. Int. Ed. *61*, e202201820. https://doi.org/10.1002/ange.202201820.
22. Li, D., Yang, J., Fang, M., Tang, B.Z., and Li, Z. (2022). Stimulus-responsive room temperature phosphorescence materials with full-color tunability from pure organic amorphous polymers. Sci. Adv. *8*, eabl8392. https://doi.org/10.1126/sciadv.abl8392.
23. Lan, R., Bao, J., Li, Z., Wang, Z., Song, C., Shen, C., Huang, R., Sun, J., Wang, Q., Zhang, L., and Yang, H. (2022). Orthogonally Integrating Programmable Structural Color and Photo-Rewritable Fluorescence in Hydrazone Photoswitch-bonded Cholesteric Liquid Crystalline Network. Angew. Chem. Int. Ed. *61*,

e202213915. https://doi.org/10.1002/anie.202213915.

24. Yu, X., Liu, K., Wang, B., Zhang, H., Qi, Y., and Yu, J. (2023). Time-Dependent Polychrome Stereoscopic Luminescence Triggered by Resonance Energy Transfer between Carbon Dots-in-Zeolite Composites and Fluorescence Quantum Dots. Adv. Mater. *35*, 2208735. https://doi.org/10.1002/adma.202208735.

25. Xu, F., and Feringa, B.L. (2023). Photoresponsive Supramolecular Polymers: From Light-Controlled Small Molecules to Smart Materials. Adv. Mater. *35*, 2204413. https://doi.org/10.1002/adma.202204413.

26. Wang, Y., Li, W., Li, M., Zhao, S., De Ferrari, F., Liscidini, M., and Omenetto, F.G. (2019). Biomaterial-Based "Structured Opals" with Programmable Combination of Diffractive Optical Elements and Photonic Bandgap Effects. Adv. Mater. *31*, 1805312. https://doi.org/10.1002/adma.201805312.

27. Lai, X., Ren, Q., Vogelbacher, F., Sha, W.E.I., Hou, X., Yao, X., Song, Y., and Li, M. (2022). Bioinspired Quasi-3D Multiplexed Anti-Counterfeit Imaging via Self-Assembled and Nanoimprinted Photonic Architectures. Adv. Mater. *34*, 2107243. https://doi.org/10.1002/adma.202107243.

28. Qi, Y., Niu, W., Zhang, S., Wu, S., Chu, L., Ma, W., and Tang, B. (2019). Encoding and decoding of invisible complex information in a dual-response bilayer photonic crystal with tunable wettability. Adv. Funct. Mater. *29*, 1906799. https://doi.org/10.1002/adfm.201906799.

29. Bian, F., Sun, L., Cai, L., Wang, Y., and Zhao, Y. (2020). Bioinspired MXene-integrated colloidal crystal arrays for multichannel bioinformation coding. Proc. Natl. Acad. Sci. USA *117*, 22736–22742. https://doi.org/10.1073/pnas.2011660117.

30. Qin, L., Liu, X., He, K., Yu, G., Yuan, H., Xu, M., Li, F., and Yu, Y. (2021). Geminate labels programmed by two-tone microdroplets combining structural and fluorescent color. Nat. Commun. *12*, 699. https://doi.org/10.1038/s41467-021-20908-y.

31. Wang, Y., Kim, B.J., Guidetti, G., and Omenetto, F.G. (2022). Generation of Complex Tunable Multispectral Signatures with Reconfigurable Protein-Based, Plasmonic-Photonic Crystal Hybrid Nanostructures. Small *18*, 2201036. https://doi.org/10.1002/smll.202201036.

32. Tang, D., Shao, Z., Zhou, Y., Lei, Y., Chen, L., Xie, J., Zhang, X., Xie, X., Fan, F., Liao, L., and Wen, S. (2022). Simultaneous surface display and holography enabled by flat liquid crystal elements. Laser Photon. Rev. *16*, 2100491. https://doi.org/10.1002/lpor.202100491.

33. Chen, K., Xu, C., Zhou, Z., Li, Z., Chen, P., Zheng, G., Hu, W., and Lu, Y. (2022). Multifunctional liquid crystal device for grayscale pattern display and holography with tunable spectral-response. Laser Photon. Rev. *16*, 2100591. https://doi.org/10.1002/lpor.202100591.

34. Zhang, Y., Le, X., Jian, Y., Lu, W., Zhang, J., and Chen, T. (2019). 3D fluorescent hydrogel origami for multistage data security protection. Adv. Funct. Mater. *29*, 1905514. https://doi.org/10.1002/adfm.201905514.

35. Zhu, C.N., Bai, T., Wang, H., Ling, J., Huang, F., Hong, W., Zheng, Q., and Wu, Z.L. (2021). Dual-encryption in a shape-memory hydrogel with tunable fluorescence and reconfigurable architecture. Adv. Mater. *33*, 2102023. https://doi.org/10.1002/adma.202102023.

36. Mondia, J.P., Amsden, J.J., Lin, D., Negro, L.D., Kaplan, D.L., and Omenetto, F.G. (2010). Rapid nanoimprinting of doped silk films for enhanced fluorescent emission. Adv. Mater. *22*, 4596–4599. https://doi.org/10.1002/adma.201001238.

37. Amsden, J.J., Domachuk, P., Gopinath, A., White, R.D., Negro, L.D., Kaplan, D.L., and Omenetto, F.G. (2010). Rapid nanoimprinting of silk fibroin films for biophotonic applications. Adv. Mater. *22*, 1746–1749. https://doi.org/10.1002/adma.200903166.

38. Wang, Y., Aurelio, D., Li, W., Tseng, P., Zheng, Z., Li, M., Kaplan, D.L., Liscidini, M., and Omenetto, F.G. (2017). Modulation of multiscale 3D lattices through conformational control: painting silk inverse opals with water and light. Adv. Mater. *29*, 1702769. https://doi.org/10.1002/adma.201702769.

39. Wang, Y., Kim, B.J., Peng, B., Li, W., Wang, Y., Li, M., and Omenetto, F.G. (2019). Controlling silk fibroin conformation for dynamic, responsive, multifunctional, micropatterned surfaces. Proc. Natl. Acad. Sci. USA *116*, 21361–21368. https://doi.org/10.1073/pnas.1911563116.

40. Zhou, Z., Zhang, S., Cao, Y., Marelli, B., Xia, X., and Tao, T.H. (2018). Engineering the future of silk materials through advanced manufacturing. Adv. Mater. *30*, 1706983. https://doi.org/10.1002/adma.201706983.

41. Guidetti, G., d'Amone, L., Kim, T., Matzeu, G., Mogas-Soldevila, L., Napier, B., Ostrovsky-Snider, N., Roshko, J., Ruggeri, E., and Omenetto, F.G. (2022). Silk materials at the convergence of science, sustainability, healthcare, and technology. Appl. Phys. Rev. *9*, 011302. https://doi.org/10.1063/5.0060344.

42. Li, C., Guo, C., Fitzpatrick, V., Ibrahim, A., Zwierstra, M.J., Hanna, P., Lechtig, A., Nazarian, A., Lin, S.J., and Kaplan, D.L. (2019). Design of biodegradable, implantable devices towards clinical translation. Nat. Rev. Mater. *5*, 61–81. https://doi.org/10.1038/s41578-019-0150-z.

43. Li, Z., Liu, Y., Marin, M., and Yin, Y. (2020). Thickness-dependent wrinkling of PDMS films for programmable mechanochromic responses. Nano Res. *13*, 1882–1888. https://doi.org/10.1007/s12274-020-2617-z[.

44. Wu, K., Zhu, T., Zhu, L., Sun, Y., Chen, K., Chen, J., Yuan, H., Wang, Y., Zhang, J., Liu, G., et al. (2022). Reversible mechanochromisms via manipulating surface wrinkling. Nano Lett. *22*, 2261–2269. https://doi.org/10.1021/acs.nanolett.1c04494.

45. Qi, Y., Zhang, S., and Lu, A.-H. (2022). Responsive structural colors derived from geometrical deformation of synthetic nanomaterials. Small Struct. *3*, 2200101. https://doi.org/10.1002/sstr.202200101.

46. Pappu, R., Recht, B., Taylor, J., and Gershenfeld, N. (2002). Physical one-way functions. Science *297*, 2026–2030. https://doi.org/10.1126/science.1074376.

47. Arppe, R., and Sørensen, T.J. (2017). Physical unclonable functions generated through chemical methods for anti-counterfeiting. Nat. Rev. Chem *1*, 0031. https://doi.org/10.1038/s41570-017-0031.

48. Zhong, D., Liu, J., Xiao, M., Xie, Y., Shi, H., Liu, L., Zhao, C., Ding, L., Peng, L.-M., and Zhang, Z. (2022). Twin physically unclonable functions based on aligned carbon nanotube arrays. Nat. Electron. *5*, 424–432. https://doi.org/10.1038/s41928-022-00787-x.

49. Leem, J.W., Kim, M.S., Choi, S.H., Kim, S.-R., Kim, S.-W., Song, Y.M., Young, R.J., and Kim, Y.L. (2020). Edible unclonable functions. Nat. Commun. *11*, 328. https://doi.org/10.1038/s41467-019-14066-5.

50. Liu, Y., Han, F., Li, F., Zhao, Y., Chen, M., Xu, Z., Zheng, X., Hu, H., Yao, J., Guo, T., et al. (2019). Inkjet-printed unclonable quantum dot fluorescent anti-counterfeiting labels with artificial intelligence authentication. Nat. Commun. *10*, 2409. https://doi.org/10.1038/s41467-019-10406-7.

51. Wang, J., Zhang, Q., Chen, R., Li, J., Wang, J., Hu, G., Cui, M., Jiang, X., Song, B., and He, Y. (2021). Triple-layer unclonable anti-counterfeiting enabled by huge-encoding capacity algorithm and artificial intelligence authentication. Nano Today *41*, 101324. https://doi.org/10.1016/j.nantod.2021.101324.

52. Yang, Y., Li, Q., Zhang, H., Liu, H., Ji, X., and Tang, B.Z. (2021). Codes in code: AIE supramolecular adhesive hydrogels store huge amounts of information. Adv. Mater. *33*, 2105418. https://doi.org/10.1002/adma.202105418.

53. Tan, J., Li, Q., Meng, S., Li, Y., Yang, J., Ye, Y., Tang, Z., Qu, S., and Ren, X. (2021). Time-dependent phosphorescence colors from carbon dots for advanced dynamic information encryption. Adv. Mater. *33*, 2006781. https://doi.org/10.1002/adma.202006781.

54. Li, M., Wang, Y., Chen, A., Naidu, A., Napier, B.S., Li, W., Rodriguez, C.L., Crooker, S.A., and Omenetto, F.G. (2018). Flexible magnetic composites for light-controlled actuation and interfaces. Proc. Natl. Acad. Sci. USA *115*, 8119–8124. https://doi.org/10.1073/pnas.1805832115.

55. Wang, Y., Li, M., Chang, J.-K., Aurelio, D., Li, W., Kim, B.J., Kim, J.H., Liscidini, M., Rogers, J.A., and Omenetto, F.G. (2021). Light-activated shape morphing and light-tracking materials using biopolymer-based programmable photonic nanostructures. Nat. Commun. *12*, 1651. https://doi.org/10.1038/s41467-021-21764-6.

56. Rockwood, D.N., Preda, R.C., Yücel, T., Wang, X., Lovett, M.L., and Kaplan, D.L. (2011). Materials fabrication from Bombyx mori silk fibroin. Nat. Protoc. *6*, 1612–1631. https://doi.org/10.1038/nprot.2011.379.